Within-subject combination of diffusion tensor MRI and CLARITY reveals alterations in the social brain network resulting from α-neurexin II deletion

Supplemental Material

Eleftheria Pervolaraki Ph.D, Adam Tyson MRes, Francesca Pibiri MSc, Steven L. Poulter Ph.D, Amy C. Reichelt Ph.D, R. John Rodgers Ph.D, Steven J. Clapcote Ph.D, Colin Lever Ph.D, Laura Andreae M.D. Ph.D, James Dachtler Ph.D

Supplemental Materials and Methods

Diffusion Tensor MRI

Data Acquisition

Brain MR imaging was performed on a vertical 9.4 Tesla spectrometer (Bruker AVANCE II NMR, Ettlingen, Germany) with an 89 mm wide bore, 3 radio frequency channels with digital broadband frequency synthesis (6-620 MHz) and an imaging coil with diameter of 25 mm for hydrogen (1H). 3D images for each brain were obtained using a DT-MRI protocol (TE: 35 ms, TR: 700 ms, 10 signal averages). The field of view was set at 128 x 128 x 128, with a cubic resolution of 100 µm/pixel and a b value of 1200 s/mm^2. For each brain, diffusion weighted images were obtained in 6 directions, based upon recent published protocols[1-5]. The subject of the number of diffusions gradients has been debated[6], with studies suggesting limited benefits of using more than 6 directions in biological tissue[7-9]. The imaging time for each brain was 60 hours.

Image Processing

Parsing of the raw data was semi-automated using DSI Studio, in order to obtain b-values for every normalized gradient vector on the x, y and z orientations. Unwanted background, setting a threshold, smoothing of the data and definition of tissue boundaries was performed prior to the reconstruction of the final 3D image. DTI analysis parameters were calculated as previously described[10].

The *ex vivo* mouse brain 3D diffusion-weighted images were reconstructed from the Bruker binary file using DSI Studio (http://dsi-studio.labsolver.org)[11]. Direction Encoded Colour Map (DEC) images were generated by combining the information from the primary eigenvectors, diffusion images and the FA. Images of the primary vectors and their orientation were reconstructed and superimposed on corresponding FA images to guide the segmentation of discrete anatomical locations according to the brain atlas (Figure 1B-D). Region of interest definition was performed by author EP and corroborated independently by JD, with region area compared between the experimenters (data not shown). The DSI Studio DTI reconstruction characterizes the major diffusion direction of the fibre within the brain[12 12, 13]. Extraction of FA (calculated [14]) and ADC was performed within selected segmented brain areas for every 3D reconstructed mouse brain.

Regions of Interest (ROIs)

Given the strong social impairments found within Nrxn2α mice, for the current study, we identified the brain regions of interest (ROIs) most closely linked with social behavior, using previously published reports of brain region involvement in social behaviour. Quantification of c-Fos immunoreactivity has highlighted the importance of several amygdala nuclei (including the basolateral) following social exposure[15], but also the anterior cingulate cortex (ACC), prefrontal cortex and the hippocampus [16]. Lesions to the primate amygdala alter social interactions[17, 18], and amygdala neurons in primates including humans increase firing rates during social scenarios[19-21]. Consistent with these animal studies, amygdala damage in humans[22] and amygdala dysfunction in ASD patients[23] impair social responses. Other socially-important brain regions have also been proposed. Notably, several studies have implicated the rodent hippocampus in social behavior, including social memory and sociability[24-26]. For instance, intrahippocampal administration of neurolide-2, which interacts with α-neurexin, specifically impairs sociability, but not anxiety and spatial learning in rats[27]. These findings are consistent with reports of social deficits in humans with hippocampal damage[28] and hippocampal abnormalities in ASD[29, 30]. Finally, several studies link the frontal cortex, particularly the orbitofrontal cortex, which is strongly anatomically connected with the amygdala[31], to social processing[32, 33], consistent with findings of abnormalities in orbitofrontal cortex in ASD[31, 34]. Control regions of the primary motor cortex (M1), primary sensory cortex (S1) and the barrel field were chosen for CLARITY (Supp. Figure 7N-O).

CLARITY

Solutions:

Hydrogel solution: 2% PFA 2% acrylamide 0.05% bis-acrylamide and 0.25% VA-044 thermal initiator (2,2'-Azobis[2-(2-imidazolin-2-yl) propane] dihydrochloride) in PBS, pH 7.4.

Clearing buffer: 8% Sodium dodecyl sulfate in 200mM boric acid, pH 8.5.

Multiphoton imaging – methodological outline

Cleared samples were mounted in custom 3D printed chambers for two-photon imaging. Images were acquired using ZEN Black (Zeiss, Germany). DAPI signal was detected using a 485 nm short pass filter, and neurofilament using a 500-550 nm band pass filter. The power of the excitation laser was varied to maximise the dynamic range for each image, but all other parameters were kept constant. The images were analysed using custom MATLAB (version 9.1, The Mathworks Inc.) scripts. Two-dimensional images were visualised using ImageJ[35] and three-dimensional images using Vaa3D[36].

Multiphoton imaging and analysis – image analysis method

Pre-processing

Image files were loaded into MATLAB (The Mathworks Ltd.) using the BioFormats toolbox[37], and the raw image data were obtained along with the precise voxel dimensions from the metadata. Each two-dimensional (2D) image from the three-dimensional (3D) stack was initially corrected for uneven background illumination by element-wise division by a 2D reference image. This reference image was calculated as the mean 2D image through the 3D stack, which was smoothed using a 2D Gaussian kernel with a full-width at half maximum (FWHM) of 20 % of the geometric mean of the dimensions of the 2D image (mean dimension). The image was denoised by filtering the image with a Gaussian kernel with a standard deviation of one pixel. Background subtraction was carried out by subtracting a smoothed, filtered image (FWHM 10 % of the mean dimension). Each pixel was then smoothed using a 3D Gaussian kernel with FWHM of 1.5 µm (the largest axonal diameter expected according to Perge et al.[38].

Segmentation

The numerical gradient of the image in each dimension $(\Delta X, \Delta Y, \Delta Z)$ was calculated, and these were combined to calculate the magnitude of the gradient $\left(\sqrt{\Delta X^2 + \Delta Y^2 + \Delta Z^2}\right)$. The resulting image was thresholded, using a combination of the Otsu (1979) and Rosin (2001) methods (Rosin threshold + 2/5 Otsu threshold)[39, 40]. The gradient image highlights the edge of each axon; to combine these into a single object, the image was dilated and then eroded with a cubic structuring element (each side being 1.5 µm, to 'close' the largest axons as per Perge et al.[38]).

Very small objects (less than 50 μm^3) were removed from the image as they reflected noise, very small neuronal processes and gradients around cells.

Owing to variations in staining intensity of different axons, the thresholding produced segmented axons of various thicknesses that did not necessarily reflect the true structure. To remove this bias, the thresholded image was skeletonised using a homotopic thinning algorithm[41] implemented in MATLAB[42]. The resulting image was dilated and then eroded using a cubic structuring element (10 pixels on each side for dilation, 9 for erosion) to produce connected processes with a uniform two-pixel diameter. This dilation ensured that the voxels in the binary image were connected via their faces (6-connected) rather than just their corners (26-connected), which better reflects the true structure of biological processes. This method detects most large axons at the expense of smaller processes, and the loss of any information about axon diameter. These steps are outlined in Supp. Figure 1.

Analysis

The density of axons was calculated as the fraction of the image volume taken up by the segmented axons. A measure of axonal alignment was calculated by determining the mean axonal alignment along each dimension. This alignment was calculated by moving along the 3D image in a single dimension, keeping the coordinates in the other dimensions constant, and counting the number of times the pixel intensity did not change (i.e. how many times an axon was not entered or left). This number was averaged across each face of the image volume and scaled to the length of each dimension to produce a metric of how constant the image intensity is in that dimension. The perfect case of no intensity change (i.e. all axons are aligned perfectly with a particular dimension) gives a value of 1. The greater the difference between this measure in each three dimensions, the more aligned the axons must be (i.e. their directions are anisotropic). The standard deviation of this measure across the three dimensions was calculated as the axonal alignment.

The alignment calculation is illustrated in Supp. Figure 2 for a simple, two-dimensional case. Supp. Figure 2a shows the case of low axonal alignment, and Supp. Figure 2b shows the case of high axonal alignment. In each case, for illustration, each pixel represented by a small square on the grid is classed as either containing an axon or not. In the real images, the pixels are smaller, and are actually binary. In each axis, the number of pixel transitions in which the presence of an axon

does not change is divided by the number of transitions, and the average is calculated. The standard deviation of this average for all axes is the measure of axonal alignment. When the alignment is low, the two averages are similar, and the standard deviation is low. When the alignment is high the two averages are very different, and the standard deviation is high. To analyse the real data, this same calculation is carried out in 3D, but in a much larger grid of voxels. Cell density was calculated as the number of cells per mm^3.

Supp. Table 1

Brain Region	DTI Measure	ANOVA Comparison	F Value	P Value
Anterior Hippocampus	FA	Genotype	$F_{(1,10)} = 3.91$	P = 0.063
		Hemisphere	$F_{(1,10)} = 3.89$	P = 0.065
Mid Hippocampus	FA	Genotype	$F_{(1,10)} = 3.12$	P = 0.07
		Hemisphere	$F_{(1,10)} < 1$	P = 0.146
Posterior Hippocampus	FA	Genotype	$F_{(1,10)} = 1.99$	P = 0.104
		Hemisphere	$F_{(1,10)} = 1.95$	P = 0.101
Anterior Hippocampus	ADC	Genotype	$F_{(1,10)} = 3.17$	P = 0.073
		Hemisphere	$F_{(1,10)} = 2.20$	P = 0.095
Mid Hippocampus	ADC	Genotype	$F_{(1,10)} < 1$	P = 0.160
		Hemisphere	$F_{(1,10)} = 1.62$	P = 0.115
Posterior Hippocampus	ADC	**Genotype**	**$F_{(1,10)} = 8.88$**	**P = 0.036**
		Hemisphere	$F_{(1,10)} < 1$	P = 0.180
Anterior Hippocampus	AD	Genotype	$F_{(1,10)} < 1$	P = 0.187
		Hemisphere	$F_{(1,10)} = 1.07$	P = 0.121
Mid Hippocampus	AD	Genotype	$F_{(1,10)} < 1$	P = 0.153
		Hemisphere	$F_{(1,10)} = 1.04$	P = 0.124
Posterior Hippocampus	AD	Genotype	$F_{(1,10)} = 3.45$	P = 0.07
		Hemisphere	**$F_{(1,10)} = 6.19$**	P = 0.052
Anterior Hippocampus	RD	Genotype	$F_{(1,10)} = 3.03$	P = 0.086
		Hemisphere	$F_{(1,10)} < 1$	P = 0.137
Mid Hippocampus	RD	Genotype	$F_{(1,10)} < 1$	P = 0.140
		Hemisphere	$F_{(1,10)} = 1.33$	P = 0.119
Posterior Hippocampus	RD	**Genotype**	**$F_{(1,10)} = 10.83$**	**P = 0.027**
		Hemisphere	$F_{(1,10)} = 3.48$	P = 0.07

Statistical analysis of the anterior (Bregma -1.94 mm), mid (Bregma -2.46 mm) and posterior (Bregma -3.28 mm) hippocampus for fractional anisotropy (FA), apparent diffusion coefficient (ADC), axial diffusion (AD) and radial diffusion (RD). Analysis was performed using repeated measure two-way ANOVAs for genotype and hemisphere (Benjamini-Hochberg corrected (corrected P values stated)).

Supp. Table 2

Brain Region	DTI Measure	ANOVA Comparison	F Value	P Value
Amygdala-Anterior Hippocampus	AD	Genotype	$F_{(1,10)}$ <1	P = 0.164
		Hemisphere	$F_{(1,10)}$ = 2.10	P = 0.097
		Genotype x Hemisphere	**$F_{(1,10)}$ = 12.12**	**P = 0.023**
Amygdala-Anterior Hippocampus	RD	Genotype	$F_{(1,10)}$ <1	P = 0.149
		Hemisphere	$F_{(1,10)}$ = 1.32	P = 0.106
		Genotype x Hemisphere	$F_{(1,10)}$ <1	P = 0.155
Amygdala-Posterior Hippocampus	AD	Genotype	$F_{(1,10)}$ <1	P = 0.142
		Hemisphere	$F_{(1,10)}$ <1	P = 0.189
		Genotype x Hemisphere	$F_{(1,10)}$ = 4.54	P = 0.061
Amygdala-Posterior Hippocampus	RD	Genotype	$F_{(1,10)}$ <1	P = 0.151
		Hemisphere	$F_{(1,10)}$ <1	P = 0.135
		Genotype x Hemisphere	$F_{(1,10)}$ <1	P = 0.128
BLA-Anterior Hippocampus	AD	Genotype	$F_{(1,10)}$ <1	P = 0.167
		Hemisphere	**$F_{(1,10)}$ = 6.59**	**P = 0.047**
		Genotype x Hemisphere	**$F_{(1,10)}$ = 10.53**	**P = 0.032**
BLA-Anterior Hippocampus	RD	Genotype	$F_{(1,10)}$ <1	P = 0.158
		Hemisphere	$F_{(1,10)}$ = 2.59	P = 0.092
		Genotype x Hemisphere	$F_{(1,10)}$ <1	P = 0.173
BLA-Posterior Hippocampus	AD	Genotype	$F_{(1,10)}$ <1	P = 0.169
		Hemisphere	**$F_{(1,10)}$ = 12.79**	**P = 0.018**
		Genotype x Hemisphere	**$F_{(1,10)}$ = 12.97**	**P = 0.02**
BLA-Posterior Hippocampus	RD	Genotype	$F_{(1,10)}$ <1	P = 0.162
		Hemisphere	$F_{(1,10)}$ = 3.11	P = 0.077
		Genotype x Hemisphere	$F_{(1,10)}$ <1	P = 0.178

Statistical analysis of the anterior (Bregma -1.94 mm), and posterior (Bregma -3.28 mm) amygdala-hippocampal connections, analysed for axial diffusion (AD) and radial diffusion (RD). Analysis was performed using repeated measure two-way ANOVAs for genotype and hemisphere (Benjamini-Hochberg corrected (corrected P values stated)).

Supp. Table 3

Brain Region	CLARITY Measure	ANOVA Comparison	F Value	P Value
M1	OI	Genotype	$F_{(1,10)}$ <1	P = 0.182
		Hemisphere	$F_{(1,10)}$ = 1.74	P = 0.108
M1	Cell Density	Genotype	$F_{(1,10)}$ = 2.04	P = 0.099
		Hemisphere	$F_{(1,10)}$ = 1.41	P = 0.117
M1	Fibre Density	Genotype	$F_{(1,10)}$ <1	P = 0.171
		Hemisphere	$F_{(1,10)}$ <1	P = 0.176
S1	OI	Genotype	$F_{(1,10)}$ <1	P = 0.185
		Hemisphere	**$F_{(1,10)}$ = 36.86**	**P = 0.005**
S1	Cell Density	Genotype	$F_{(1,10)}$ <1	P = 0.131
		Hemisphere	**$F_{(1,10)}$ = 13.73**	**P = 0.016**
S1	Fibre Density	Genotype	$F_{(1,10)}$ = 1.73	P = 0.110
		Hemisphere	**$F_{(1,10)}$ = 8.51**	**P = 0.038**
BF	OI	Genotype	$F_{(1,10)}$ <1	P = 0.191
		Hemisphere	**$F_{(1,10)}$ = 10.59**	**P = 0.034**
BF	Cell Density	Genotype	$F_{(1,10)}$ <1	P = 0.133
		Hemisphere	**$F_{(1,10)}$ = 8.70**	**P = 0.041**
BF	Fibre Density	Genotype	$F_{(1,10)}$ <1	P = 0.144
		Hemisphere	$F_{(1,10)}$ <1	P = 0.126

Statistical analysis of the primary motor cortex (M1), primary somatosensory cortex (S1) and the barrel field (BF). CLARITY imaged regions were then analysed for orientation index (OI), cell density and fibre density. Analysis was performed using repeated measure two-way ANOVAs for genotype and hemisphere (Benjamini-Hochberg corrected (corrected P values stated)).

Supp. Figure 1.

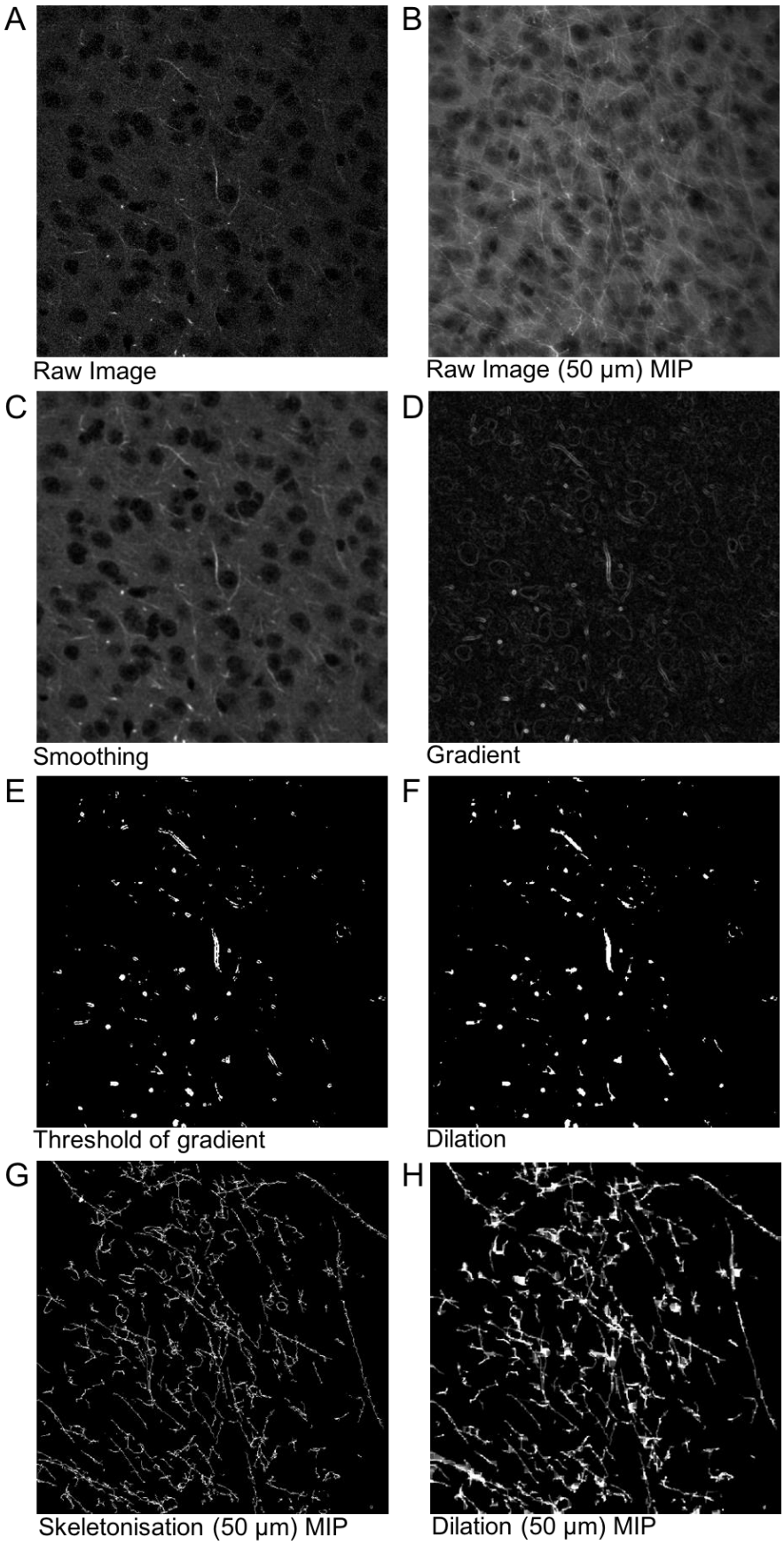

Analysis methodology of axonal segmentation from multiphoton images.

Supp. Figure 2

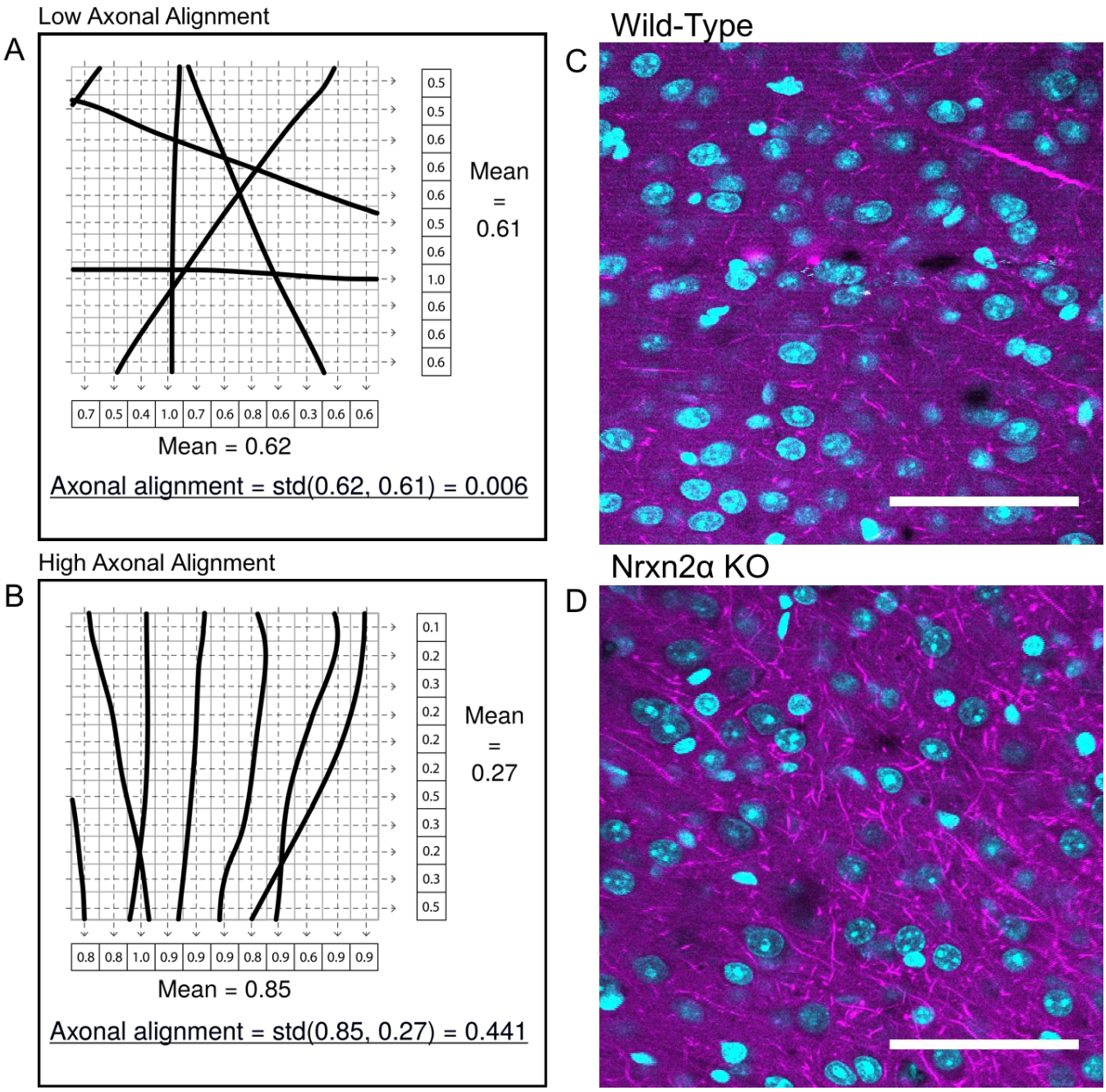

A and B. Illustration of the axonal alignment calculation in a simple two-dimensional case. The grey grid represents the image pixels, the black lines axons and the dashed lines represent the calculation process. Standard deviation denoted as std. **C and D.** Cingulate cortex images taken from wild-type and Nrxn2α KO mice, visually representing the greater axonal alignment and density in KO mice.

Supp. Figure 3

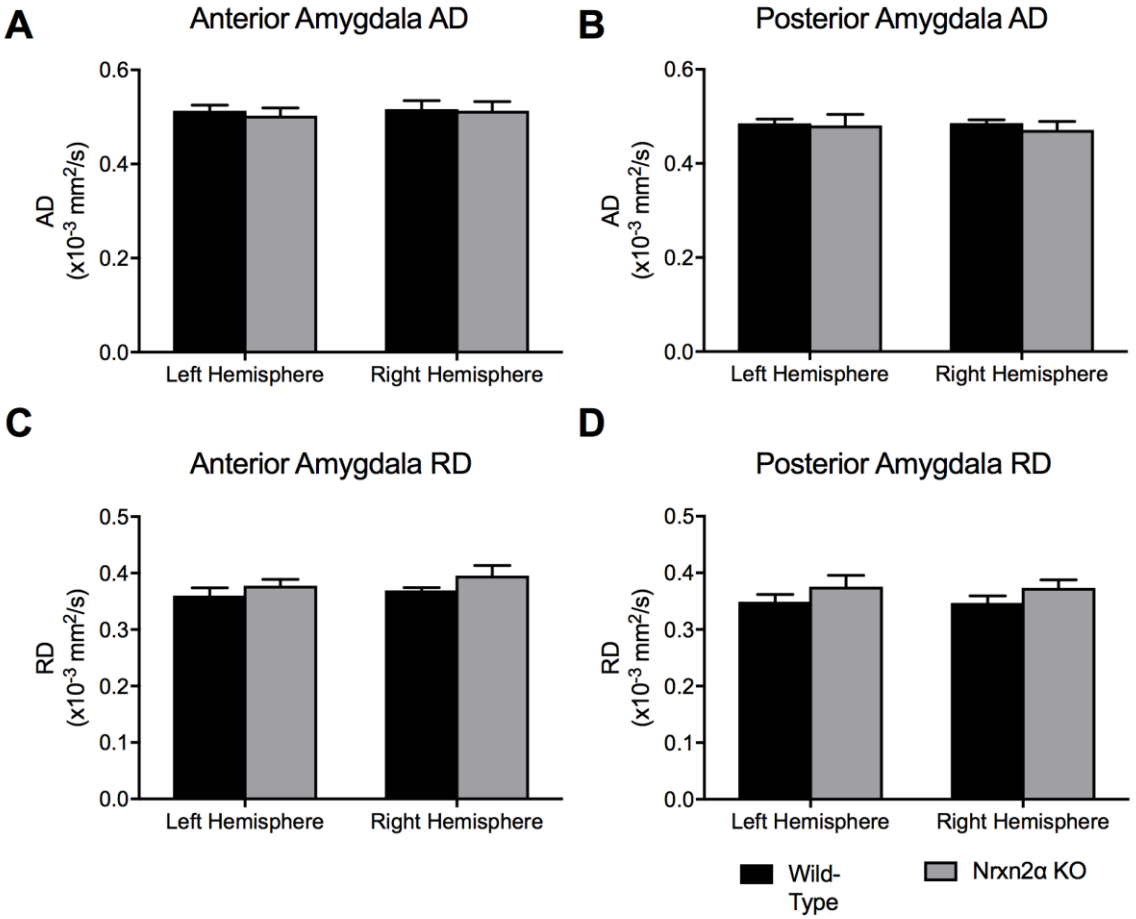

Axial diffusivity (AD) and radial diffusivity (RD) in the amygdala. The entire amygdala was segmented from DTI images at two regions; anterior (**A** and **C**: Bregma -1.94 mm) and posterior (**B** and **D**: Bregma -2.46 mm). No significant differences were observed between the genotypes for anterior or posterior regions. Error bars represent s.e.m. Wild-type n=6, Nrxn2α KO n=6.

Supp. Figure 4

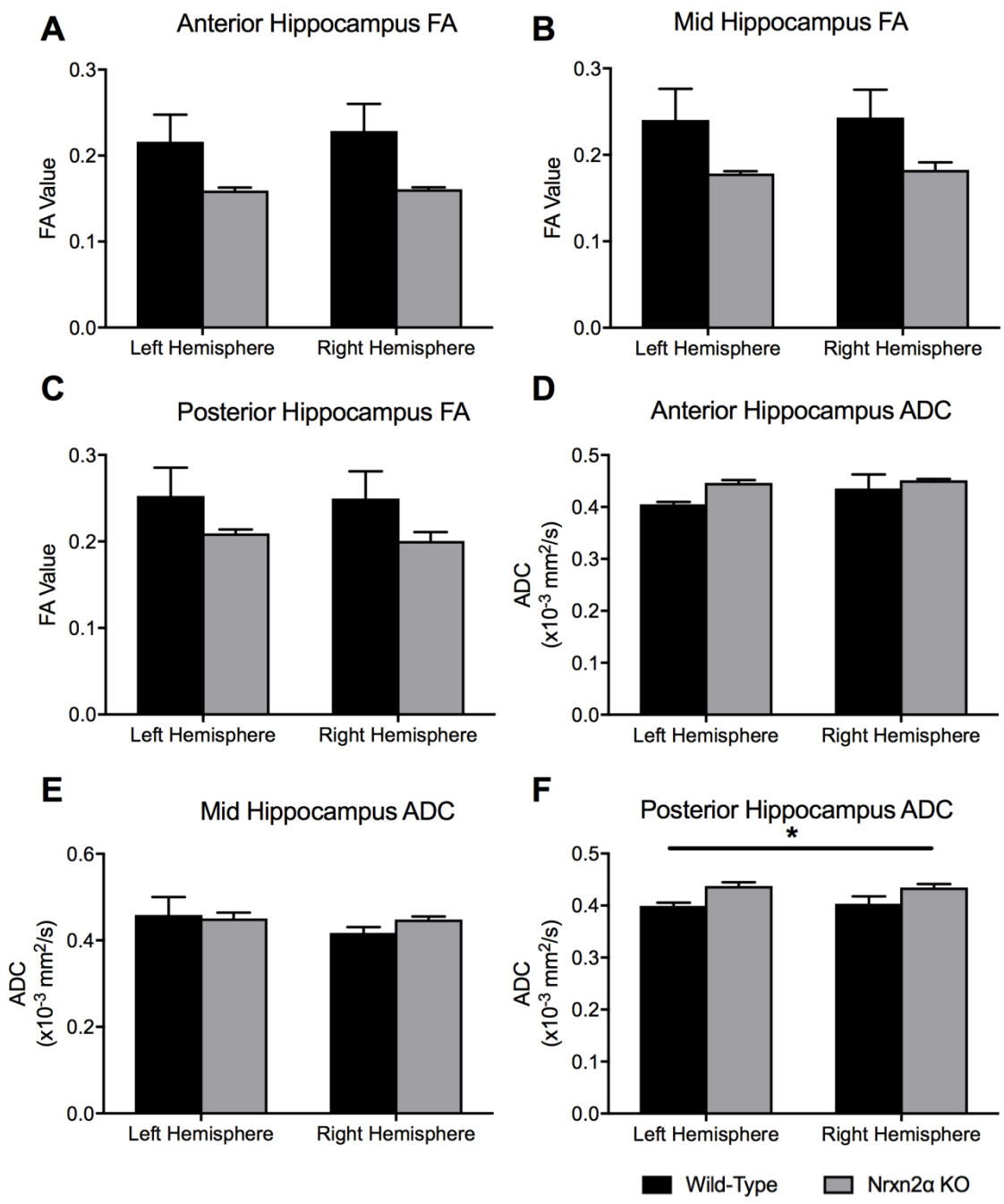

Fractional anisotropy (FA) and apparent diffusion coefficient (ADC) of the anterior to posterior hippocampus. Although Nrxn2α KO had trends towards lower FA in the anterior (**A**), mid (**B**) and posterior (**C**) hippocampus, there were no significant differences. Similarly, anterior (**D**) and mid (**E**) hippocampal regions did not vary between the genotypes, the posterior hippocampus (**F**) had significantly increased ADC (f). * = P<0.05. Error bars represent s.e.m. Wild-type n=6, Nrxn2α KO n=6.

Supp. Figure 5

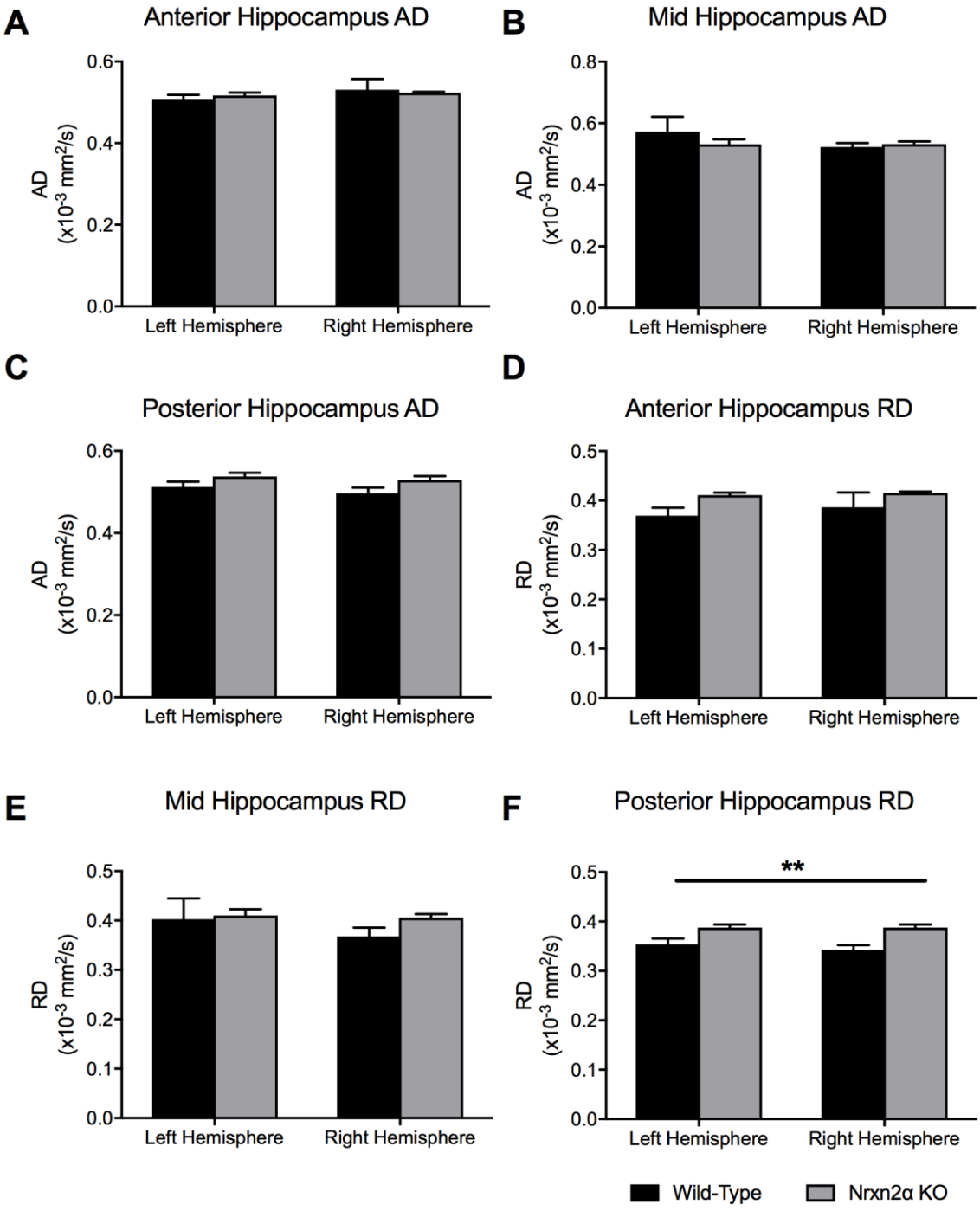

Axial diffusivity (AD) and radial diffusivity (RD) of the anterior to posterior hippocampus. AD did not differ in either the anterior (**A**), mid (**B**) and posterior (**C**) hippocampus. Although the anterior (**D**) and mid (**E**) hippocampal regions did not vary between the genotypes, the posterior hippocampus (**F**) had significantly increased RD (f). ** = P<0.01. Error bars represent s.e.m. Wild-type n=6, Nrxn2α KO n=6.

Supp. Figure 6

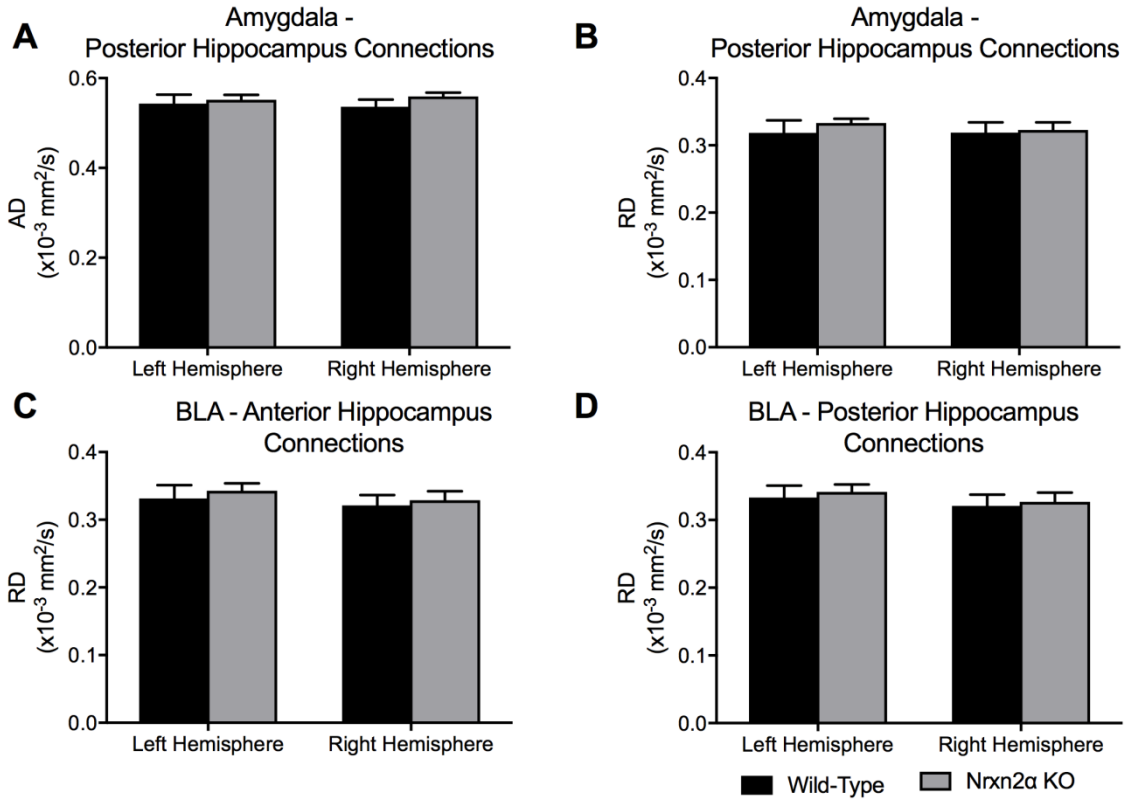

Axial diffusivity (AD) and radial diffusivity (RD) of computed tracts of connections from the amygdala to hippocampus. Tracts from the anterior amygdala to the posterior hippocampus (Bregma -2.46 mm) were analysed for AD (**A**) and RD (**B**). No significant differences between the tracts of Nrxn2α KO mice were observed. No significant differences were found for RD of tracts specifically from the basolateral nuclei of the amygdala (BLA) to the anterior (**C**) or posterior (**D**) hippocampus. Error bars represent s.e.m. Wild-type n=6, Nrxn2α KO n=6.

Supp. Figure 7

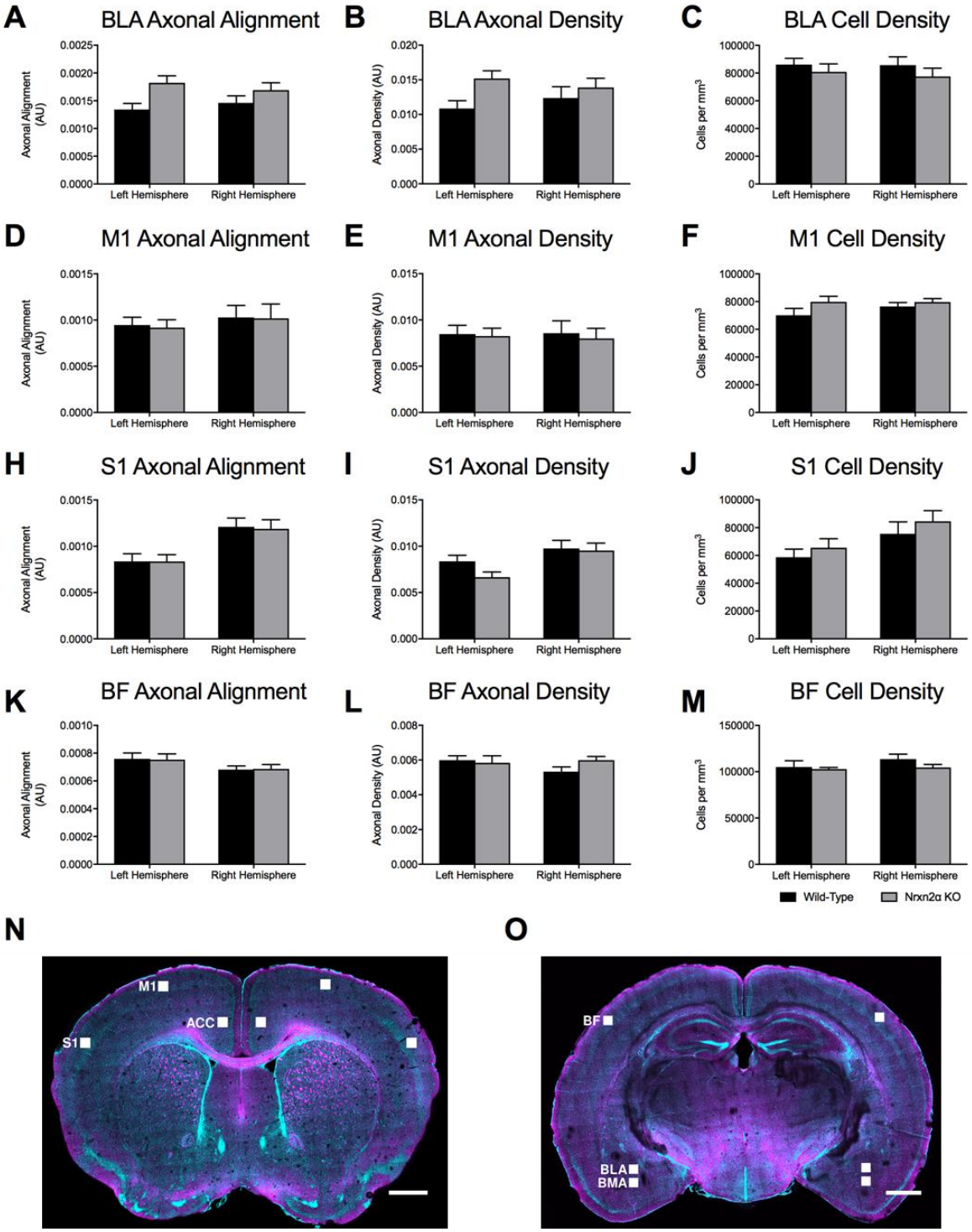

CLARITY-derived quantification of fibres and cell density within the basolateral amygdala (BLA). (**A**) Although there were trends towards increased axonal alignment and fibre density (**B**) in Nrxn2α KO mice, no significant differences were found. (**C**) Cell density in the BLA was similar between the genotypes. Statistical analysis (Supp. Table 4) was performed for the primary motor cortex (M1; **D-F**), primary somatosensory cortex (S1; **H-J**) and the barrel field (BF; **K-M**). No genotypic differences were found for any measure within these cortical regions. (N-O)

CLARITY images of the scanned regions of interest. Error bars represent s.e.m. Wild-type n=6, Nrxn2α KO n=6.

References

1. Wu D, Xu J, McMahon MT, van Zijl PC, Mori S, Northington FJ, *et al*. In vivo high-resolution diffusion tensor imaging of the mouse brain. *NeuroImage* 2013; **83:** 18-26.

2. Vo A, Sako W, Dewey SL, Eidelberg D, Ulug AM. 18FDG-microPET and MR DTI findings in Tor1a+/- heterozygous knock-out mice. *Neurobiology of disease* 2015; **73:** 399-406.

3. Kumar M, Duda JT, Hwang WT, Kenworthy C, Ittyerah R, Pickup S, *et al*. High resolution magnetic resonance imaging for characterization of the neuroligin-3 knock-in mouse model associated with autism spectrum disorder. *PloS one* 2014; **9**(10)**:** e109872.

4. Ruest T, Holmes WM, Barrie JA, Griffiths IR, Anderson TJ, Dewar D, *et al*. High-resolution diffusion tensor imaging of fixed brain in a mouse model of Pelizaeus-Merzbacher disease: comparison with quantitative measures of white matter pathology. *NMR in biomedicine* 2011; **24**(10)**:** 1369-1379.

5. Kim S, Pickup S, Fairless AH, Ittyerah R, Dow HC, Abel T, *et al*. Association between sociability and diffusion tensor imaging in BALB/cJ mice. *NMR in biomedicine* 2012; **25**(1)**:** 104-112.

6. Jones DK. The effect of gradient sampling schemes on measures derived from diffusion tensor MRI: a Monte Carlo study. *Magnetic resonance in medicine* 2004; **51**(4)**:** 807-815.

7. Lebel C, Benner T, Beaulieu C. Six is enough? Comparison of diffusion parameters measured using six or more diffusion-encoding gradient directions with deterministic tractography. *Magnetic resonance in medicine* 2012; **68**(2)**:** 474-483.

8. Ni H, Kavcic V, Zhu T, Ekholm S, Zhong J. Effects of number of diffusion gradient directions on derived diffusion tensor imaging indices in human brain. *AJNR American journal of neuroradiology* 2006; **27**(8)**:** 1776-1781.

9. Hasan KM, Parker DL, Alexander AL. Comparison of gradient encoding schemes for diffusion-tensor MRI. *Journal of magnetic resonance imaging : JMRI* 2001; **13**(5)**:** 769-780.

10. Pervolaraki E, Dachtler J, Anderson RA, Holden AV. Ventricular myocardium development and the role of connexins in the human fetal heart. *Scientific reports* 2017; **7**(1)**:** 12272.

11. Yeh FC, Verstynen TD, Wang Y, Fernandez-Miranda JC, Tseng WY. Deterministic diffusion fiber tracking improved by quantitative anisotropy. *PloS one* 2013; **8**(11)**:** e80713.

12. Basser PJ, Mattiello J, LeBihan D. Estimation of the effective self-diffusion tensor from the NMR spin echo. *Journal of magnetic resonance Series B* 1994; **103**(3)**:** 247-254.

13. Jiang H, van Zijl PC, Kim J, Pearlson GD, Mori S. DtiStudio: resource program for diffusion tensor computation and fiber bundle tracking. *Computer methods and programs in biomedicine* 2006; **81**(2)**:** 106-116.

14. Pervolaraki E, Anderson RA, Benson AP, Hayes-Gill B, Holden AV, Moore BJ, *et al*. Antenatal architecture and activity of the human heart. *Interface focus* 2013; **3**(2)**:** 20120065.

15. Ferguson JN, Aldag JM, Insel TR, Young LJ. Oxytocin in the medial amygdala is essential for social recognition in the mouse. *The Journal of neuroscience : the official journal of the Society for Neuroscience* 2001; **21**(20)**:** 8278-8285.

16. Tanimizu T, Kenney JW, Okano E, Kadoma K, Frankland PW, Kida S. Functional Connectivity of Multiple Brain Regions Required for the Consolidation of Social Recognition Memory. *The Journal of neuroscience : the official journal of the Society for Neuroscience* 2017; **37**(15)**:** 4103-4116.

17. Emery NJ, Capitanio JP, Mason WA, Machado CJ, Mendoza SP, Amaral DG. The effects of bilateral lesions of the amygdala on dyadic social interactions in rhesus monkeys (Macaca mulatta). *Behavioral neuroscience* 2001; **115**(3)**:** 515-544.

18. Rosvold HE, Mirsky AF, Pribram KH. Influence of amygdalectomy on social behavior in monkeys. *Journal of comparative and physiological psychology* 1954; **47**(3)**:** 173-178.

19. Mosher CP, Zimmerman PE, Gothard KM. Neurons in the monkey amygdala detect eye contact during naturalistic social interactions. *Current biology : CB* 2014; **24**(20)**:** 2459-2464.

20. Rutishauser U, Mamelak AN, Adolphs R. The primate amygdala in social perception - insights from electrophysiological recordings and stimulation. *Trends in neurosciences* 2015; **38**(5)**:** 295-306.

21. Rutishauser U, Tudusciuc O, Wang S, Mamelak AN, Ross IB, Adolphs R. Single-neuron correlates of atypical face processing in autism. *Neuron* 2013; **80**(4)**:** 887-899.

22. Adolphs R, Tranel D, Damasio AR. The human amygdala in social judgment. *Nature* 1998; **393**(6684)**:** 470-474.

23. Baron-Cohen S, Ring HA, Bullmore ET, Wheelwright S, Ashwin C, Williams SC. The amygdala theory of autism. *Neuroscience and biobehavioral reviews* 2000; **24**(3)**:** 355-364.

24. Maaswinkel H, Baars AM, Gispen WH, Spruijt BM. Roles of the basolateral amygdala and hippocampus in social recognition in rats. *Physiology & behavior* 1996; **60**(1)**:** 55-63.

25. Kogan JH, Frankland PW, Silva AJ. Long-term memory underlying hippocampus-dependent social recognition in mice. *Hippocampus* 2000; **10**(1)**:** 47-56.

26. Okuyama T, Kitamura T, Roy DS, Itohara S, Tonegawa S. Ventral CA1 neurons store social memory. *Science* 2016; **353**(6307)**:** 1536-1541.

27. van der Kooij MA, Fantin M, Kraev I, Korshunova I, Grosse J, Zanoletti O, *et al*. Impaired hippocampal neuroligin-2 function by chronic stress or synthetic peptide treatment is linked to social deficits and increased aggression. *Neuropsychopharmacology : official publication of the American College of Neuropsychopharmacology* 2014; **39**(5)**:** 1148-1158.

28. Rubin RD, Watson PD, Duff MC, Cohen NJ. The role of the hippocampus in flexible cognition and social behavior. *Frontiers in human neuroscience* 2014; **8:** 742.

29. Nicolson R, DeVito TJ, Vidal CN, Sui Y, Hayashi KM, Drost DJ, *et al*. Detection and mapping of hippocampal abnormalities in autism. *Psychiatry research* 2006; **148**(1)**:** 11-21.

30. Schumann CM, Hamstra J, Goodlin-Jones BL, Lotspeich LJ, Kwon H, Buonocore MH, *et al*. The amygdala is enlarged in children but not adolescents with autism; the hippocampus is enlarged at all ages. *The Journal of neuroscience : the official journal of the Society for Neuroscience* 2004; **24**(28)**:** 6392-6401.

31. Bachevalier J, Loveland KA. The orbitofrontal-amygdala circuit and self-regulation of social-emotional behavior in autism. *Neuroscience and biobehavioral reviews* 2006; **30**(1)**:** 97-117.

32. Beer JS, John OP, Scabini D, Knight RT. Orbitofrontal cortex and social behavior: integrating self-monitoring and emotion-cognition interactions. *Journal of cognitive neuroscience* 2006; **18**(6)**:** 871-879.

33. Watson KK, Platt ML. Social signals in primate orbitofrontal cortex. *Current biology : CB* 2012; **22**(23)**:** 2268-2273.

34. Girgis RR, Minshew NJ, Melhem NM, Nutche JJ, Keshavan MS, Hardan AY. Volumetric alterations of the orbitofrontal cortex in autism. *Progress in neuro-psychopharmacology & biological psychiatry* 2007; **31**(1)**:** 41-45.

35. Schindelin J, Arganda-Carreras I, Frise E, Kaynig V, Longair M, Pietzsch T, *et al*. Fiji: an open-source platform for biological-image analysis. *Nature methods* 2012; **9**(7)**:** 676-682.

36. Peng H, Ruan Z, Long F, Simpson JH, Myers EW. V3D enables real-time 3D visualization and quantitative analysis of large-scale biological image data sets. *Nature biotechnology* 2010; **28**(4)**:** 348-353.

37. Linkert M, Rueden CT, Allan C, Burel JM, Moore W, Patterson A, *et al*. Metadata matters: access to image data in the real world. *The Journal of cell biology* 2010; **189**(5)**:** 777-782.

38. Perge JA, Niven JE, Mugnaini E, Balasubramanian V, Sterling P. Why do axons differ in caliber? *The Journal of neuroscience : the official journal of the Society for Neuroscience* 2012; **32**(2)**:** 626-638.

39. Otsu N. A Threshold Selection Method from Gray-Level Histograms. *IEEE Transactions on Systems, Man, and Cybernetics* 1979; **9**(1)**:** 62-66.

40. Rosin P. Unimodal thresholding. *Pattern Recognition* 2001; **34**(11)**:** 2083-2096.

41. Lee T, Kashyap R, Chu C. Building Skeleton Models via 3-D Medial Surface Axis Thinning Algorithms. *CVGIP: Graphical Models and Image Processing* 1994; **56**(6)**:** 462-478.

42. Kerschnitzki M, Kollmannsberger P, Burghammer M, Duda GN, Weinkamer R, Wagermaier W, *et al*. Architecture of the osteocyte network correlates with bone material quality. *Journal of bone and mineral research : the official journal of the American Society for Bone and Mineral Research* 2013; **28**(8)**:** 1837-1845.